














Optimization of Plasmonic-Organic Hybrid Electro-Optics

B. H. Robinson , L. E. Johnson , D. L. Elder , A. A. Kocherzhenko, C. M. Isborn , C. Haffner , W. Heni ,
C. Hoessbacher , Y. Fedoryshyn, Y. Salamin , B. Baeuerle , A. Josten , M. Ayata, U. Koch ,
J. Leuthold , *Fellow, IEEE*, and L. R. Dalton , *Senior Member, IEEE*

(Invited Paper)

Abstract—Plasmonic-organic hybrid technology affords the potential for exceptional bandwidth, extremely small footprint, and very low drive voltages resulting in substantially improved energy efficiency for devices. Optical loss is a well-recognized problem for plasmonic technologies but is currently addressed with some notable success. Thereby, the optimization of electrically poled organic electro-optic (OEO) materials is most critical since a large electro-optical coefficient allows implementation of short active device structures that result in lower insertion losses and lower voltage-length products. Most importantly, short structures also guarantee largest bandwidths and best energy efficiencies. Yet, an efficient optimization of in-device performance of OEO materials requires the development of novel computational simulation methods, especially as waveguide width dimensions reach tens of nanometers in plasmonic waveguides and as electrode surface/material interfacial effects become more and more dominant. The focus of this communication is on novel multi-scale modeling methods, including coarse-grained Monte Carlo statistical mechanical simulations combined with quantum mechanical methods to simulate and analyze the linear and nonlinear optical properties for high chromophore number density solid-state OEO materials. New chromophores are developed with the assistance of theory and may lead to an order of magnitude improvement in device performance.

Manuscript received January 30, 2018; revised July 24, 2018; accepted August 9, 2018. Date of publication August 17, 2018; date of current version October 19, 2018. This work was supported in part by the National Science Foundation under Grant DMR-1303080 and in part by the Air Force Office of Scientific Research under Grant FA9550-15-1-0319. The work of A. A. Kocherzhenko and C. M. Isborn was supported by the U.S. Department of Defense (67310-CH-REP) under the AFOSR Organic Materials Division and the NSF MRI program (ACI-1429830 and ACI-1429783). The work of C. Haffner, W. Heni, C. Hoessbacher, Y. Fedoryshyn, Y. Salamin, B. Baeuerle, A. Josten, M. Ayata, U. Koch, and J. Leuthold was supported in part by the EU-project PLASMOFab (688166) and in part by the ERC PLASILOR project (670478). (*Corresponding author: Larry R. Dalton.*)

B. H. Robinson, L. E. Johnson, D. L. Elder, and L. R. Dalton are with the Department of Chemistry and Electrical Engineering, University of Washington, Seattle, WA 98196-1700 USA (e-mail: bhrobin@uw.edu; lewisj@uw.edu; elderdl@uw.edu; larryd@uw.edu).

A. A. Kocherzhenko and C. M. Isborn are with the Department of Chemistry and Chemical Biology, University of California–Merced, Merced, CA 95343 USA (e-mail: akocherzhenko@ucmerced.edu; cisborn@ucmerced.edu).

C. Haffner, W. Heni, C. Hoessbacher, Y. Fedoryshyn, Y. Salamin, B. Baeuerle, A. Josten, M. Ayata, U. Koch, and J. Leuthold are with the Institute of Electromagnetic Fields, Swiss Federal Institute of Technology (ETH Zurich), Zurich 8092, Switzerland (e-mail: haffnerc@ethz.ch; wheni@ethz.ch; choessbacher@ethz.ch; yuriy@ief.ee.ethz.ch; salamin@ethz.ch; bbaeuerle@ethz.ch; ajosten@ethz.ch; mayata@ethz.ch; uelikoch@ethz.ch; JuergLeuthold@ethz.ch).

Color versions of one or more of the figures in this paper are available online at <http://ieeexplore.ieee.org>.

Digital Object Identifier 10.1109/JLT.2018.2865882

Index Terms—Interfacial interactions, multi-scale theoretical methods, organic electro-optic materials, plasmonic-organic hybrid (POH) devices, poling-induced acentric and centric order.

I. INTRODUCTION

ELECTRO-OPTIC (EO) modulators have long been recognized as important components of integrated electronic-photonics devices relevant to telecommunications, computing, sensor technology, and metrology [1]–[3]. A research objective of growing interest is the reduction of the size mismatch between electronic and photonic circuit elements, which is particularly important for the chipscale integration of electronics and photonics. The potential for chipscale integration is one of the reasons for interest in silicon photonic, photonic crystal, metamaterial, and plasmonic device architectures [4]–[62]. Other important parameters for EO modulators, include the bandwidth, the drive voltage, the energy efficiency, and the optical insertion loss. Among the many types of modulators, plasmonic devices stand out because of the potential for exceptionally small footprints ($\sim 1 \mu\text{m}^2$). If combined with an ultrafast nonlinear optical effect material, they also offer extremely high bandwidths ($> 1 \text{ THz}$) as the configuration affords extremely low RC time constants. Organic electro-optic (OEO) materials are a most favorable choice as they offer extremely high bandwidths, e.g., bandwidths of 15 THz have been demonstrated and even higher bandwidths are likely possible [62]. OEO materials are Pockels effect materials and the phase relaxation time (a few femtoseconds) of the conjugated π -electron system of OEO materials determines the intrinsic bandwidth response. Electrical resistance in traditional dielectric modulators typically limits bandwidths to values much smaller than can potentially be achieved with OEO materials [62]. Thus, the integration of OEO materials into plasmonic device architectures affords a unique opportunity for realizing high bandwidth devices. A second important advantage of OEO materials is the potential for engineering of materials for exceptional electro-optic activity. The electro-optic activity of OEO materials is proportional to the molecular first hyperpolarizability (β) of its constituent chromophores, the number density (ρ_N) of those chromophores, and the extent to which the chromophores are acentrically ordered ($\langle \cos^3 \theta \rangle$) parallel to the direction of the applied electric fields (RF, optical, and poling). The EO activity, characterized by the EO coefficient (r_{33}),

is discussed in detail in the Appendix. If the β of current generation chromophores could be translated completely (perfect order) into macroscopic EO activity, the resulting electro-optic coefficients would be considerably greater than 1000 pm/V, approximately 50 times that of lithium niobate. A third, but not well appreciated, advantage of OEO materials is that, through solvent casting, they are easily integrated into diverse (silicon photonic, plasmonic, photonic crystal, and metamaterial) device architectures [10]–[25], [32]–[54], [57]–[62]. Thus, OEO materials afford the opportunity for very inexpensive development of circuits with large-scale-integration of modulators. A challenge with respect to the use of OEO materials is thermal and photochemical stability when low glass transition temperature (T_g) polymeric (e.g., guest-host chromophore-polymer) composites are utilized. This deficiency has been effectively addressed by lattice hardening (chromophore crosslinking) protocols that commonly exploit Diels-Alder cycloaddition chemistry [62]–[65]. Of course, OEO materials will never compete with the thermal stability that can be achieved with metal oxide materials at extremely high temperatures. However, such extremely harsh conditions (temperatures above 400 °C) generally rule out the use of CMOS electronics as well; and ultra-high temperature stability is not a relevant concern for many electronic-photonic integration applications. Power handling capability is also related to material glass transition temperature (due to suppression of singlet oxygen mechanisms of photodegradation), and utilization of power levels typical for telecommunication presents no problem with respect to the use of hardened OEO materials [62], [66], [67].

As has been noted elsewhere [43], in-device electro-optic activity (r_{33}) has a profound effect on voltage-length ($U_\pi L$, i.e., the product of the voltage U_π required to achieve a phase shift of π and the length L of the device, i.e., electrode length) performance, energy efficiency, and optical insertion loss. For POH devices, three factors determine $U_\pi L$: (1) The fundamental EO activity of the material, (2) the electric field confinement and enhancement associated with nanoscopic device dimensions (e.g., electrode separations), and (3) the “slow light” effect associated with the propagation of surface plasmon polaritons [35], [43]. Recently, and contrary to initial expectation, $U_\pi L$ has been observed to increase with decreasing electrode separation below 120 nm [41], [43]. Since large electro-optic activity permits small $U_\pi L$ values (e.g., the present best value is on the order of 40 V- μ m [43]) and since low $U_\pi L$ values are critical to achieving small device footprints and for facilitating acceptable optical insertion loss, optimization of in-device electro-optic activity is important for the practical utilization of POH technology. For these reasons, a key research objective has been the theory-assisted design of new OEO materials with not only dramatically improved EO activity but also auxiliary properties such as desired linear optical properties, viscoelasticity, and ultimately thermal/photochemical stability. The effort directed toward this goal has resulted in an order of magnitude improvement in r_{33} values since 2000 and more importantly has also resulted in a paradigm shift in the development of electrically-poled OEO materials. Prior to the present theory-assisted development paradigm, OEO materials were low number density

chromophore-polymer composite materials or chromophores covalently attached to traditional polymers such as polymethylmethacrylates (PMMA), polycarbonates (PCs), and polyimides (PIs) at low to modest number densities [62]. However, coarse-grained Monte Carlo calculations have shown that improved EO activity can be obtained with high number density neat chromophore materials [49], [68]–[70]. Moreover, such simulations, and corresponding experiments, have shown that EO activity can be enhanced by reduction of the matrix dimensionality (the rotational degrees of freedom experienced by EO chromophores during electric field poling [71]–[73]). This observation has, in turn, led to the development of new processing protocols such as laser assisted electric field poling [74]. Theory-assisted OEO material development has also led to an enhanced ability to improve poling-induced acentric and centric order through a systematic implementation of concepts such as site isolation, matrix dimensionality control, optimization of the chromophore number density-acentric order tradeoff, and avoidance of kinetic trapping during poling by systematic chromophore modification to control intermolecular interactions with resultant influence on poling-induced acentric and centric order [49], [68]–[70]. Theory has also illustrated the role of chromophore molecular symmetry on poling-induced order and the importance of carefully considering the impact on chromophore number density for any putative chromophore modification.

Advances in the application of combined quantum and statistical mechanical simulations have been required to elucidate structure/function relationships critical to optimizing the performance of POH devices. Because fully atomistic statistical mechanical calculations [49], [62] are not computationally efficient enough to simulate the electric field poling process for a realistic number of OEO chromophores in a timely manner, coarse-grained statistical mechanical methods and new simulation protocols have been developed to appropriately treat OEO materials under electric field poling conditions. For example, to model the chromophores with an efficient number of coarse-grained structural elements, ellipsoids have proven more accurate than spheres for representing π -electron segments such as the cores of OEO chromophores, phenyl groups, etc. Such modification has also been shown to be important for coarse-grained modeling of highly polar liquids [75] and liquid mixtures involving quadrupolar interactions between aromatic moieties [76]. Also, using multiple ellipsoids, to represent features such as the curvature (non-linearity) of chromophore cores, has been required to increase the level of detail in representing a chromophore while achieving the best possible computational efficiency (shortest simulation time). This feature is embedded in the Level of Detail (LOD) protocol that has been recently introduced for systematic generation of coarse-grained structures [49], [68]–[70]. Finally, efficient convergence of simulations to the correct global energy minimum is important for the systems where such an equilibrium condition is realized experimentally. Acceleration of the convergence of simulations has been achieved with introduction of the Adiabatic Volume Adjustment (AVA) method, which mimics the condensation of molecules from a less dense phase to a higher-density phase (e.g., solution

to a solid) [49], [68]–[70]. When simulations using AVA convergence acceleration are compared to more traditional NPT (constant temperature and pressure) or NVT (constant density and temperature) simulations performed without any convergence acceleration, insight can be gained into the kinetic trapping of chromophores in local energy minima, resulting in configurations that favor centrosymmetric order and low acentric order. In like manner, quantum mechanical calculations have been tested and extended to determine accurate techniques for the simulation of many-atom OEO chromophores. Hybrid density functional theory (DFT) methods require adjustment of the amount of exact exchange to realize adequate prediction of relative molecular first hyperpolarizabilities of chromophores considered for development [77], [78]. Consideration of dielectric permittivity effects is also important when computing molecular first hyperpolarizabilities [79]. Most recently, quantum mechanical methods that account for excitonic interactions between chromophores have been developed and benchmarked for evaluating the linear and nonlinear optical properties of chromophore aggregates obtained from coarse-grained statistical simulations of high number density OEO materials [80].

Coarse-grained Monte Carlo simulations have provided the theoretical basis and motivation for the paradigm shift from low number density to high number density materials and have emphasized the importance of considering the impact of any modification of chromophore structure on number density. In turn, the importance of developing modifications that serve multiple purposes (site isolation, matrix dimensionality control, matrix hardness, viscoelasticity control) is emphasized to minimize unwanted reduction of chromophore number density associated with specific modifications. The paradigm shift in OEO material development has also been influenced by experimental observations. For example, when OEO materials were only used in dielectric modulator devices with lengths on the order of 1 cm, it was crucial to keep the optical propagation loss associated with OEO materials to less than 2 dB/cm. Because absorption from the overtone vibrations of hydrogen contribute about 1 dB/cm loss, this meant that the loss associated with the lowest energy electronic transitions of the chromophores had to be kept to very low values, in turn, placing limits on the lengths of chromophores that could be utilized. The red (bathochromic)-shifting of the interband transition observed with increasing chromophore length can lead to unacceptable optical loss for operation at telecommunication wavelengths (centered around 1.3 or 1.55 μm). To limit the degree of red-shifting, the length of the chromophore polyene bridge has been held constant in the current-generation chromophores, creating what has become known as CLD class chromophores. However, it has been recently shown that the contribution to propagation loss from chromophore absorption is well below that of plasmonic losses so that operation at shorter wavelengths and/or use of longer chromophores can be exploited without impact on observed total propagation loss [45]. Thus, use of longer length chromophores, together with the use of a wider range of donor and acceptor moieties, is becoming a signature of the optimization of the performance of POH devices and will be an important aspect of this communication.

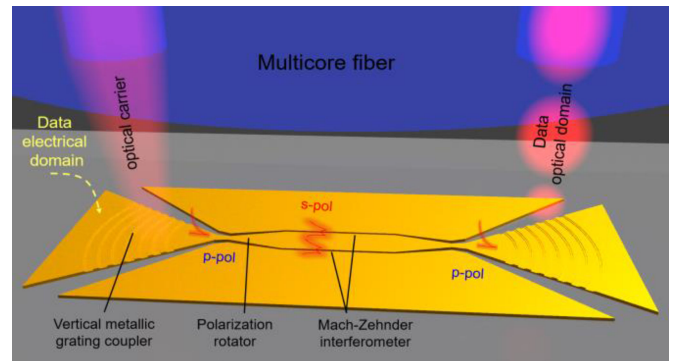


Fig. 1. An all-metallic plasmonic device is schematically illustrated showing grating coupler, polarization rotator, and Mach Zehnder modulator (integrating OEO materials). Reproduced with permission from reference [46].

As longer, more red-shifted chromophores are employed, molecular first hyperpolarizability and index of refraction will be increased. The acentric order parameter of electrically-poled OEO materials is small, typically less than 0.2. For low number density OEO materials, with isotropic index of refraction, n_{iso} , values on the order of 1.6, the anisotropy of n can be neglected in evaluating $(n_e)^3 r_{33}$ where n_e is the extraordinary index of refraction. However, as shown in this communication, this is not a good approximation for chromophores longer than CLD and for high number density chromophore materials, particularly if poling-induced order is increased beyond 0.2. Thus, an additional paradigm shift in the optimization of OEO materials is the shift to a first-principles focus on simulation of both index of refraction and electro-optic properties. Also, there is a push to develop additional methods for measurement of order parameters and the anisotropy of both electro-optic activity and index of refraction to permit a more reliable evaluation of $(n_e)^3 r_{33}$ in devices.

The focus of this communication is on optimizing the performance of OEO materials in POH devices. However, some brief comments on recent device architectures and performance demonstrations are appropriate. The state-of-the-art of POH technology is evident in the recent demonstrations and discussions of both non-resonant (phase, Mach Zehnder amplitude, In-Phase-Quadrature modulators) and resonant (ring resonators, resonant antennae) devices [32]–[54]. Typically, a metal-insulator-metal waveguide configuration is used as the active device region for both approaches. Lengths of non-resonant devices are typically 5 to 20 μm permitting optical loss as low as 8 dB to be achieved [32]–[54], [81]. As noted above, plasmonics permits small device footprints to be achieved. A recent example is shown in Figure 1 illustrating a device with a footprint of $6 \times 36 \mu\text{m}$, an area that includes couplers, polarization rotators, and the Mach-Zehnder plasmonic modulator [46]. This device permits direct integration with a multicore fiber. For PAM4 operation, the energy consumption is 33 fJ/bit at 116 Gbit/s. Other plasmonic modulators have exhibited a response beyond 170 GHz [42]. These modulators [33] have been demonstrated for NRZ operation at 100 Gbit/s with an energy efficiency of 2.8 fJ/bit [50] or PAM4 at 116 or 120 Gbit/s [42], [46].

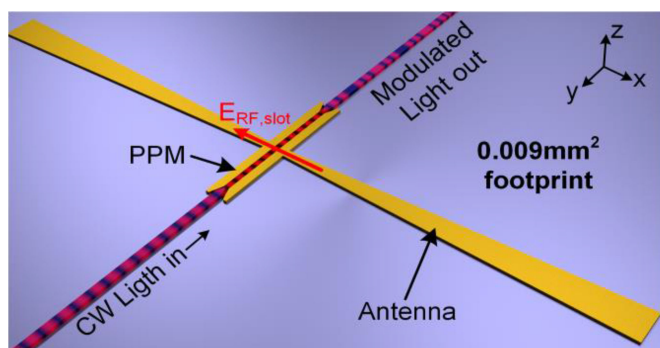


Fig. 2. A resonant antenna incorporating a plasmonic photonic modulator (PPM) is shown.

Plasmonic IQ-modulators have been demonstrated with lengths below $15 \mu\text{m}$ and tested with QAM4 modulator formats at 200 Gbit/s and QAM16 at 128 Gbit/s [51]. Power consumptions of 78 fJ/bit and 27 fJ/bit have been reported for QPSK and 16-QAM modulation formats at 144 and 72 Gbit/s, respectively [39].

Resonant approaches feature similar interaction lengths as non-resonant devices, but offer the advantage of significantly reduced insertion loss values of 2–3 dB [47].

Another important application area is that of RF photonics. RF transmitters and receivers have been demonstrated. Plasmonic resonant antennae, such as shown in Figure 2, permit direct transduction of wireless RF signals to fiber transmission without the use of electronics [37]–[40]. The resonant antenna enhances the voltage drop across the plasmonic slot resulting in a field strength increase as much as 92,000 [38]. Integration of multiple plasmonic photonic modulators (PPMs) on a chip yields plasmonic beam forming arrays for 60 GHz beamforming [40]. Beam steering settling times below 50 ps have been observed and symbol-by-symbol beam steering of 10 GBd [82] and 1 GBd [40] has been demonstrated.

II. THEORY-ASSISTED DESIGN OF OEO MATERIALS

A. Development and Application of Statistical Mechanical Theoretical Methods

The greatest potential advantage of OEO materials may be the ability to dramatically alter material properties by chemical modification of chromophore structure. The problem is that many competing interactions of comparable magnitude must be understood to realize, in a timely manner, improvement of performance of OEO materials in devices. Structure/function relationships are exceedingly complex and numerical simulation using high performance computing is required for a quantitative or even semi-quantitative understanding of POH device performance. Protocols have been developed to use state-of-the-art quantum and statistical mechanical computational methods to realize effective theory-assisted design of new materials. As noted in the preceding section, coarse-graining using ellipsoids, the LOD method, and the AVA protocol have been required to gain a quantitative understanding of electro-optic activity in

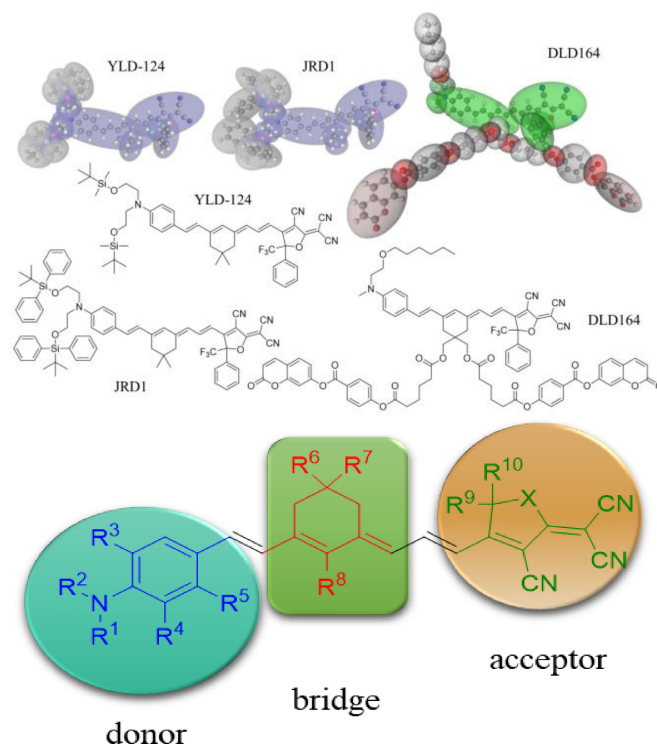


Fig. 3. The chemical structures (middle) and coarse-grained Monte Carlo representations (top) of three of the most commonly used chromophores are shown. Bottom: The donor (blue), bridge (red), and acceptor (green) moieties of a CLD-class chromophore are illustrated, along with potential substitution points.

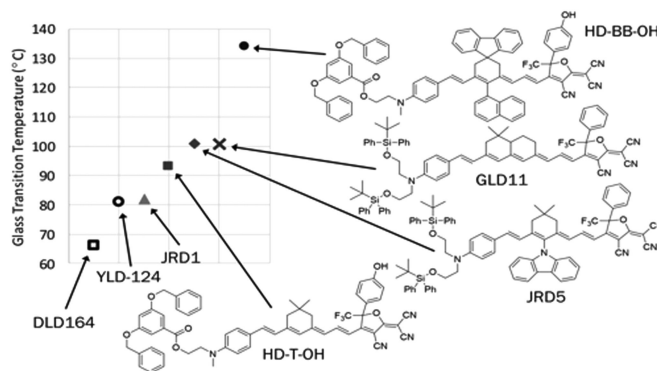


Fig. 4. Recently synthesized chromophores indicate the effect of structure modification on material glass transition temperature. With the exception of GLD11, all chromophores shown are CLD-type, i.e., have bridges of comparable length.

POH devices. In the following, we discuss a number of current and new materials. We illustrate structures of chromophores most relevant to the current communication in Figures 3 and 4.

Figure 3 shows the coarse-grained description of chromophores at an LOD = 2 level (Note that LOD refers to the number of ellipsoids used to represent the chromophore core; additional ellipsoids are also used to represent substituents attached to the core). Figure 4 illustrates several common chromophore modifications and shows the impact of these modifications on material glass transition (for uncrosslinked materials).

As can be seen from Figures 3 and 4, OEO chromophores consist of an electron rich “donor” and an electron deficient “acceptor” connected by a π -electron “bridge”.

The chromophore HD-BB-OH is an example of a chromophore modified to promote “site isolation” or the inhibition of close side-by-side approach of chromophores (close proximity promotes centrosymmetric pairing associated with strong dipole-dipole interactions). Coarse-grained Monte Carlo simulations have shown that although the acentric order parameter continues to improve with such modification (reaching values of 0.3), addition of overly bulky pendant groups for site isolation can actually lead to a decrease in poling-induced r_{33} values. The decrease in r_{33} values results from the reduction in chromophore number density that occurs with the addition of bulky side groups. Another example of the utility of site isolation modification that exploits steric interactions is the addition of crosslinking moieties such as dienes and dienophiles used in Diels-Alder crosslinking [62]–[65]. This modification reduces chromophore number density, but the increase in acentric order (through increased site isolation) with such addition can offset this reduction, leading to similar electro-optic activity for both crosslinked and uncrosslinked materials. Simulations also reveal that optimum electro-optic activity for chromophores with dipole moments similar to CLD-class chromophores will be realized at high chromophore number density rather than at lower number density as was the case with chromophores with smaller dipole moments [62]. Coarse-grained simulations yield good reproduction of acentric order ($\langle \cos^3\theta \rangle$) and poling efficiency (r_{33}/E_p). For example, for DLD164, calculated values of $\langle \cos^3\theta \rangle$ and r_{33}/E_p are 0.17 ± 0.03 and 2.0 ± 0.3 (nm/V)² while experimental values are 0.16 ± 0.03 and 2.0 ± 0.13 (nm/V)², respectively. A more interesting comparison is between traditional NPT and AVA-accelerated simulations results for YLD-124 and for JRD1. For YLD-124, NPT gives a value for $\langle \cos^3\theta \rangle = 0.04 \pm 0.02$ while AVA-accelerated simulation yields $\langle \cos^3\theta \rangle = 0.17 \pm 0.01$. This disagreement in $\langle \cos^3\theta \rangle$ suggests a substantial propensity for kinetic trapping of YLD-124 chromophores in non-global minima during poling. For JRD1, NPT yields $\langle \cos^3\theta \rangle = 0.14 \pm 0.05$ while AVA gives $\langle \cos^3\theta \rangle = 0.22 \pm 0.03$. The AVA results for JRD1 are in agreement with experiment. Comparison suggests that the energetic barrier for kinetic trapping is smaller for JRD1 than for YLD-124. Such simulations can also provide insight into the scatter observed in poling data for some materials.

An attenuation of r_{33} , and an increase in $U_\pi L$, with decreasing waveguide width (electrode separation) is observed for widths less than 100 nm for all materials studied in POH and SOH devices [41], [43]. Simulations, shown in Figure 5 [43], incorporate electrostatic interactions between chromophores and electrode surfaces.

These preliminary stimulation results strongly support the contention that there are strong short-range interactions between chromophores and electrode surfaces and that this interaction causes chromophores to lie along the electrode surfaces (normal to the electric field poling direction). Coarse-grained Monte Carlo simulations further suggest that the transition between chromophores ordered with respect to the electrode sur-

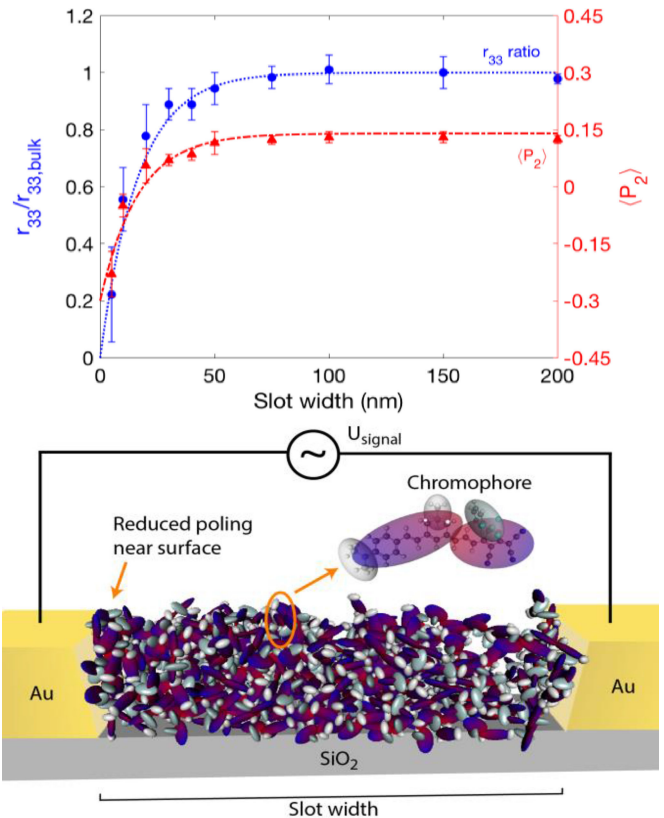


Fig. 5. Upper. Coarse-grained Monte Carlo simulation of the variation of electro-optic activity with waveguide width, w , (electrode separation) is shown (blue), along with centrosymmetric order, $\langle P_2 \rangle$ (red), which is crucial for determining birefringence. Data are re-plotted from reference [41]. Lower. A schematic cross-section of a POH waveguide, showing chromophore distribution from a coarse-grained Monte Carlo simulation at 400 K and a poling field of 100 V/um with a 20 nm waveguide (slot) width. The calculation used periodic boundary conditions on all directions other than those defined by the Au walls. Chromophores near the electrodes show reduced poling, lying flat against the electrode surface. The observed effect of the wall in the simulations is an exponential fall off (dashed lines) with a characteristic length of 16 nm. Both EO activity (proportional to acentric order) and centrosymmetric order along the poling axis show similar exponential fall offs.

faces and those exhibiting “bulk” behavior occurs over a short distance. As is to be expected because of the greater site isolation of DLD164, JRD1 exhibits greater electro-optic activity and lower $U_\pi L$ for electrode separations greater than 150 nm but DLD164 yields larger r_{33} values and lower $U_\pi L$ for the smallest separations [41]. These results indicate that interfacial interactions and the details of device architectures must be considered when nanoscopic device dimensions are involved. The results also emphasize the importance of modifying both chromophores and electrode surfaces to minimize this unwanted attenuation of electro-optic activity. Sequential synthesis/self-assembly methods [62] might also be used as an alternative to electric field poling for the narrowest widths.

As already noted, a paradigm shift in the development of OEO materials has occurred changing focus from low chromophore number density materials to high number density (neat) materials with control of intermolecular interactions through structural modification to improve acentric order. This paradigm shift has resulted in an increase in index of refraction as well as

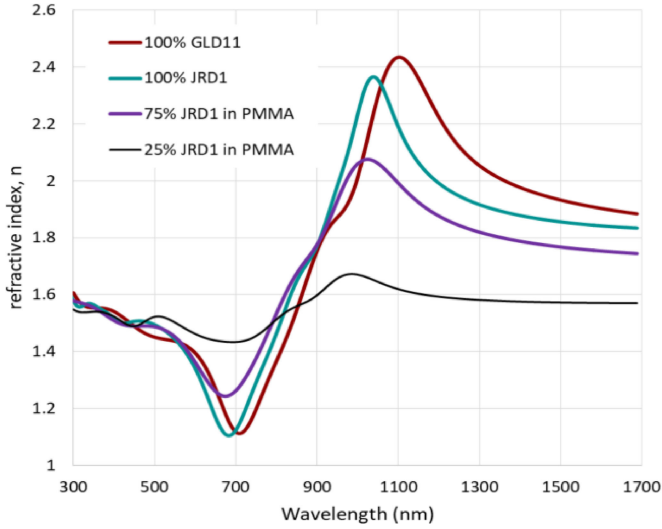


Fig. 6. The isotropic refractive index, n_{iso} , obtained from VASE experiments for unpoled samples with various concentrations of JRD1 is shown as a function of the wavelength of the optical field.

electro-optic activity. $U_{\pi}L$ depends on $(n_e)^3 r_{33}$, where n_e is the extraordinary index of refraction. In contrast, r_{33} has a weak dependence on n_e , only through the local field factors, and decreases somewhat as n_e increases.

The relation is: $\frac{U_{\pi}L}{\lambda w} \Gamma = \frac{1}{n_e^3 r_{33}}$. Γ is the combined overlap fraction of the optical field (of wavelength λ) and modulation fields with the OEO material. A detailed derivation is available in the Appendix. For low chromophore number density materials with small poling induced order, the anisotropy of the refractive index can be ignored, i.e., the values of n_e and n_o for poled materials are very near n_{iso} , values for unpoled (completely disordered or isotropic) samples. The n values of earlier guest-host OEO materials were near 1.6. The variable angle spectroscopic ellipsometry (VASE) data shown in Figure 6 illustrate the dependence of the index of refraction on chromophore concentration and on the length of the conjugated π -electron system through comparison of JRD1 and GLD11. Furthermore, DFT simulations of crystalline YLD-124 [83] at the PAW-HSE06 level of theory using a sum-over-states approach in VASP (Vienna *ab initio* Simulation Package) [84], [85] yielded a n_{\parallel} (chromophore dipole axis) of 3.31 and n_{\perp} (off-axis) of 1.54 at 1550 nm.

While these values represent maximum anisotropy due to the symmetry of the crystal, which is substantially higher than for an electrically-poled material, substantial anisotropy is projected for neat OEO materials with moderately-improved poling-induced order, as shown in Figure 7. The increasing magnitude and anisotropy of index of refraction has motivated an effort to implement first principles calculations of index of refraction and dielectric permittivity as well as electro-optic activity. This emphasizes the necessity of considering refractive index anisotropy (n_e) in analyzing $U_{\pi}L$ performance and in estimating the impact of incorporating new OEO materials into POH devices. The extraordinary index of refraction, n_e , depends on the centric order parameter $\langle P_2(\theta) \rangle$, related to $\langle \cos^2\theta \rangle$, which exhibits a quadratic dependence on E_p .

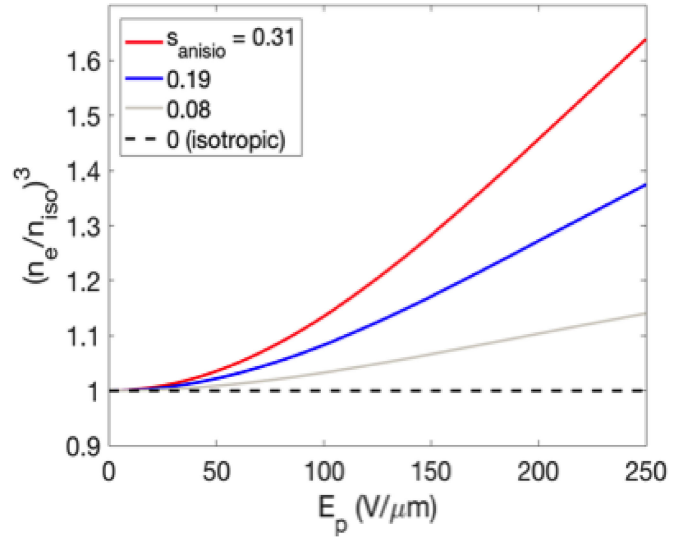


Fig. 7. Change in the extraordinary component of the refractive index of a YLD-124-like OEO material as predicted by a Langevin freely-rotating dipole model. The model assumes $\mu = 31$ D, $T_{\text{pol}} = 400$ K, $n_{\text{iso}} = 2.17$, and $\varepsilon_{\text{static}} = 8$. The highest anisotropy ratio, representing $n_{\parallel} = 3.5$, $n_{\perp} = 1.5$, is similar to that calculated for YLD-124. For $s = 0.31$ the ratio is bounded: $1 < (n_e/n_{\text{iso}})^3 < 4.3$. See Appendix for details.

The poling-field dependent ratio of n_e and n_{iso} depends on the anisotropy parameter, s , of the individual molecule (as obtained from solid-state calculations on their crystal structures): $s = \frac{n_{\parallel} - n_{\perp}}{n_{\parallel} + 2n_{\perp}}$, as $\frac{n_e}{n_{\text{iso}}} = 1 + 2s \langle P_2(\theta) \rangle$. The anisotropy ratio for YLD-124 at 1550 nm, based on the PAW-HSE06 calculated refractive indices, is 0.29 (see Appendix for details).

High refractive indices, combined with index anisotropy, may partially account for improved performance in devices using the latest materials with high values of $\langle \cos^2\theta \rangle$ (especially those recently designed and synthesized) due to reduced dimensionality and sub-100 nm waveguides. However, it should be kept in mind when considering Figure 7 that it is normally difficult to realize poling fields greater than 100 V/μm and acentric order parameters greater than 0.2. Moreover, increases in poling-induced n_e values to the present have been less than 0.2, suggesting that the contribution to $U_{\pi}L$ is in the range of 10–25%. However, for future chromophores (particularly those with longer bridges), these values could change significantly.

B. Development and Application of Quantum Mechanical Methods

Multi-scale (correlated quantum and statistical mechanics) theoretical methods start with quantum mechanical electronic structure calculations, frequently performed with hybrid density functional theory (DFT) methods. The resulting molecular properties (structures, dipole moments, and charges) are used to parameterize coarse-grained statistical mechanical simulation methods discussed in the preceding section for the computation of chromophore order (odd and even order parameters) under electric field poling. As with statistical mechanical methods, benchmarking of quantum mechanical methods is carried out with particular attention paid to correctly incorporating

dielectric permittivity and frequency dispersion effects [79]. Multi-scale methods come full circle when information about chromophore organization obtained from statistical mechanical models is fed back to quantum mechanical calculations on “chromophore clusters” to evaluate the effect of intermolecular π -electron electronic interactions [80].

Quantum mechanical methods can be used to predict the hyperpolarizability values, β , for condensed phase chromophores. All-electron calculations of the first hyperpolarizability using hybrid density functionals with exact exchange are limited to small chromophore aggregates (~ 4 YLD-124 chromophores) due to computational cost. However, we have recently shown that a computationally inexpensive quantum mechanical molecular exciton model compares well to all-electron DFT calculations for predicting the optical absorption spectra of OEO chromophore aggregates [80]. Such a model can describe the effects of both electron density polarization on individual chromophores and exciton delocalization between chromophores on the optical response of molecular aggregates. Within a two-state model (TSM) [86], [87], the molecular exciton approximation can be used to compute the first hyperpolarizability of large chromophore aggregates, making it possible to study electro-optic effects in bulk materials. Although not in all cases, the TSM can accurately compute hyperpolarizabilities of some OEO chromophores [87]. To the best of our knowledge, the TSM has not previously been used to compute of the first hyperpolarizability of chromophore aggregates.

To test the accuracy of the TSM for chromophore aggregates, we compared first hyperpolarizability values computed using the TSM to values computed using the more rigorous all-electron DFT Coupled Perturbed Hartree-Fock, CPHF method [88] on small clusters of four OEO chromophores (see Figure 8). The comparison was performed for 25 aggregates of four YLD-124 chromophores (see example in Figure 8A) selected from a coarse-grained Monte Carlo simulation of 108-chromophores. The first hyperpolarizability values calculated using the TSM from values obtained from all-electron time-dependent density functional theory calculations on the aggregate or from values using the same molecular exciton model as in [80] compare reasonably well to values calculated using CPHF on the four-chromophore aggregate (Figure 8B). The agreement with the CPHF computed hyperpolarizability is similar when using all-electron time-dependent density functional theory calculations on the aggregate or when using the same molecular exciton model as in [80]. However, even better agreement with CPHF calculations of the first hyperpolarizability for chromophore aggregates can be obtained by performing CPHF calculations on individual YLD-124 chromophores in the aggregate and summing up their contributions (Figure 8C). This good agreement suggests that higher lying states beyond the first bright state play as large of a role as excitonic interactions between chromophores in affecting the value of r_{33} for small aggregates of OEO chromophores at distances and orientations expected in semi-amorphous molecular solids. Work is underway to study these interactions for larger aggregates. Excitonic interactions likely play a larger role in determining r_{33} in highly ordered systems (such as crystals).

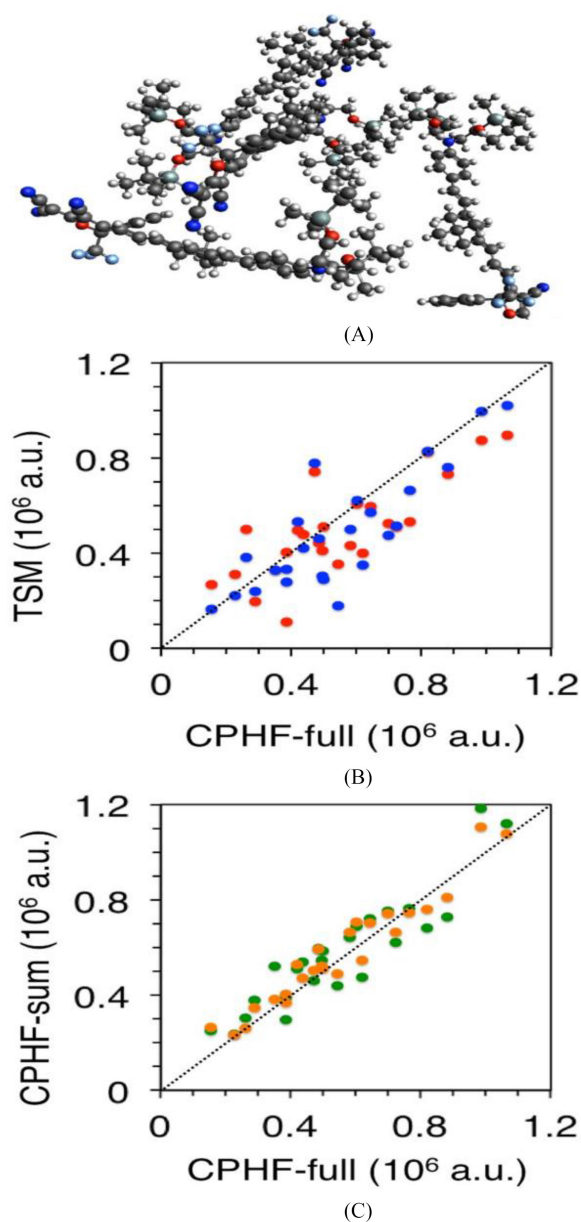


Fig. 8. Comparison of the first hyperpolarizabilities for 25 aggregates of four YLD-124 chromophores (A) selected from a Monte-Carlo snapshot as described in Ref. [80] calculated using various approximate methods to CPHF calculations on the entire aggregate (CPHF-full): (B) the TSM value for the hyperpolarizability is computed directly from all-electron TDDFT calculations on the aggregate (red) or using the same molecular exciton model [80] (blue); (C) the sum of the first hyperpolarizabilities of individual YLD-124 chromophores, calculated in isolation (green) or taking into account the polarization of the electron density by other chromophores in the aggregate, represented by ChelpG atomic charges (orange). The dotted line denotes perfect agreement between the two methods.

Calculation of the predicted relative hyperpolarizability, $\beta/\beta_{\text{reference}}$, values of individual putative chromophores is the first step in the development of new OEO materials. Examples of the insight that can be gained at this initial stage of theory-assisted design are given in Figure 9, which illustrates the variation of relative β values (referenced to YLD-124) as a function of chromophore dipole moment (also referenced to

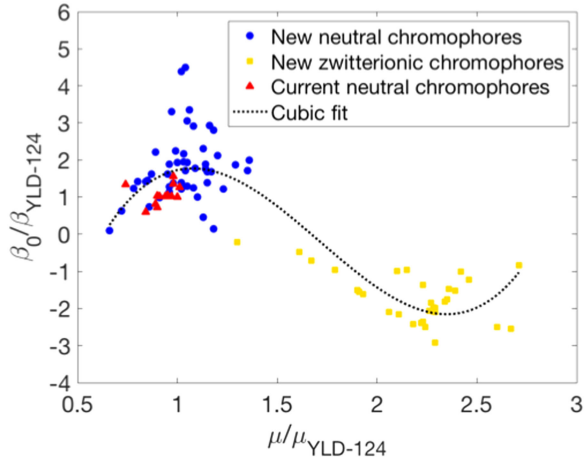


Fig. 9. Relative (vs. benchmark chromophore YLD-124) molecular first hyperpolarizability and dipole moments of existing chromophores (shown in red) and new designs (shown in blue and yellow) calculated at the M062X/6-31+G(d) level of theory in PCM chloroform are shown and plotted against each other. Two maxima are observed, one at a similar dipole moment to YLD-124, and another for zwitterionic chromophores (negative hyperpolarizability, shown in yellow) with much larger dipole moments. Because of exceptionally strong centrosymmetric aggregation, it has proven extremely difficult to pole zwitterionic chromophores. Some new chromophores (shown in blue) are predicted to exhibit 4.5 times larger β values. Reproduced from [49] with permission.

YLD-124) for both current and new chromophores (including chromophores under consideration for further development).

Theory and experiment have shown that chromophores with dipole moments significantly smaller than YLD-124 yield optimum electro-optic activity for low number density materials with the result of electro-optic coefficients, r_{33} , much smaller than that of YLD-124. For chromophores with dipole moments much greater than YLD-124 (such as the zwitterionic chromophores shown in yellow in Figure 9), centrosymmetric pairing is so strong that poling efficiency is extremely poor, resulting in minimal electro-optic activity [62].

Thus, statistical mechanical and quantum mechanical simulations and experiments suggest that YLD-124, and chromophores with similar dipole moments, lie in a sweet spot region that permits utilization of high chromophore number density materials and realization of reasonable acentric order leading to near optimum electro-optic activity. The quantum mechanical calculations shown in Figure 9 further illustrate that this region also leads to optimum molecular first hyperpolarizability β and that substantially larger hyperpolarizabilities can be obtained in this dipole moment range than for existing CLD-class chromophores.

Figure 10 provides a representative example of how tuning at a specific site, in this case, the combined effect of modifications at R_9 and R_{10} on a CLD-class chromophore (Figure 3), can lead to improvements in β . These improvements are not simply additive, but theory reveals which combinations lead to the largest molecular first hyperpolarizability and potentially electro-optic activity if chromophores can be poled with the same efficiency as current chromophores. The quantum mechanical results shown here suggest that improvements in β (and potentially r_{33}) of 4–5 are likely. Increase of n_e with some of these chromophores

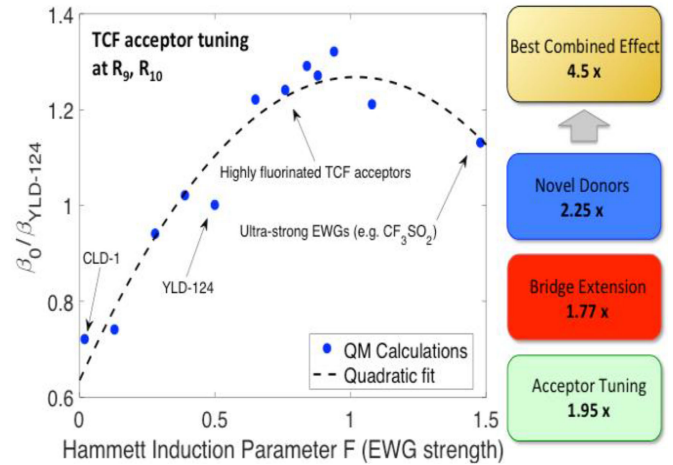


Fig. 10. A wide variety of chromophore modifications have been studied computationally using QM calculations at the M062X/6-31+G(d) level of theory in PCM chloroform, indicating particularly large potential from longer bridges, new donors, and modifications to the TCF ($X = O$) and TCP ($X = NR$) acceptors. An example tuning study for the two substitution points on the TCF acceptor is shown in the left panel. EWG stands for electron withdrawing group. Systematic tuning of chromophore components can combine to produce chromophores with performance predicted to be greatly in excess of YLD-124 (right panel). Adapted from [49] with permission.

may lead to further (but smaller, i.e., 20–25%) improvement, as may resonance enhancement effects due to red-shifting of the chromophore charge transfer band.

Recent simulations illustrate the importance of considering the refractive index anisotropy in analyzing $U_\pi L$ performance of POH devices and in estimating the performance of new materials in devices. The extraordinary index of refraction (n_e) depends on the centric order parameter, $\langle \cos^2 \theta \rangle$ or $\langle P_2 \rangle$, and exhibits a quadratic dependence on E_p .

III. SUMMARY

Multi-scale (correlated quantum and statistical mechanics) theoretical methods have been developed and applied to theory-assisted design of new OEO materials. Theory has promoted several paradigm shifts in the development of electrically-poled OEO materials including focus on neat, high chromophore number density materials where core chromophore structures are modified to achieve a number of desired properties including electro-optic activity, index of refraction, viscoelasticity, thermal and photochemical stability. When modifying chromophores, trade-offs exist between improving poling-induced acentric order, thermal/photochemical stability, and chromophore number density. Plasmonic devices permit longer chromophores to be used without negatively impacting propagation loss. Longer chromophores utilized as high number density materials exhibit increased index of refraction anisotropy under poling and this needs to be taken into account in evaluating device performance. High chromophore number densities also raise the question as to whether intermolecular π -electron interactions influence molecular first hyperpolarizability and thus electro-optic activity. Multi-scale calculations on solid state high number density OEO materials

reported here suggest that such excitonic interactions do not substantially influence macroscopic electro-optic activity for the types of chromophores considered here (i.e., only somewhat ordered OEO materials). Also, theoretical calculations suggest that chromophores under development will lead to significantly improved in-device electro-optic activity. Theory has provided considerable insight into the dependence of poling-induced order on electrode separation in plasmonic devices. Both chromophores and electrode surfaces may have to be modified to minimize attenuation of device performance for the smallest waveguide widths. Theoretically designed chromophores now under development are expected to lead to significantly improved in-device electro-optic activity. Such modification should permit dramatic reduction of $U_\pi L$ with corresponding impact on insertion loss, device footprint, and energy efficiency.

APPENDIX

Relationship of r_{33} and $U_\pi L$: There are two, completely distinct but interdependent, orientational order parameters [73], which control the amount of optical activity seen in any OEO device. These parameters are the acentric order parameter, $\langle \cos^3 \theta \rangle$ (closely related to the more common $\langle \cos \theta \rangle$) and the centrosymmetric order parameter, $\langle P_2 \rangle = \frac{1}{2}(3\langle \cos^2 \theta \rangle - 1)$. For OEO materials in waveguides (see Figures 1, 2, 5), order is introduced by the poling field of strength, E_p (and also influenced by intermolecular interactions and interaction of chromophores with surfaces). The angle θ is the angle between the chromophore dipole moment and the poling field. The values of the order parameters upon poling are dependent on the properties of the chromophores. The poling field tends to force some alignment of the chromophores, with their dipoles oriented perpendicular to the electrodes of POH devices or rails of SOH devices. Much of the following is discussed in further detail by Kuzyk and co-workers in Ref. 87.

Poling is conducted at temperatures near the glass transition temperature of the material and then locked in by cooling and/or crosslinking. This poling process, as applied to the Pockels effect OEO materials, defines and sets the elements of the EO tensor, \tilde{r} (as the k^{th} component of the full EO tensor) through the dielectric tensor, ε , as it relates to the second order susceptibility tensor, $\chi^{(2)}$:

$$\varepsilon \tilde{r} \varepsilon = -2\chi^{(2)}(-\omega; \omega, 0) \quad (1)$$

The principal element is $r_{33} \equiv \tilde{r}_{3,3,3}$. The dielectric tensor, $\tilde{\varepsilon}$, is generally considered to be diagonal and the absorption parts are considered to be small. With respect to poling induced order, the fundamental definition of the electro-optic tensor, \tilde{r} , shows that it is primarily dependent on the acentric order of the chromophores and is weakly dependent on the solid-state dielectric constant of the OEO material. For example:

$$r_{33} = -2g(\omega) N\beta(-\omega; \omega, 0) \langle \cos^3 \theta \rangle \quad (2)$$

where $g(\omega) = \frac{f_\omega^2 f_o}{n_\omega^2} = \left(\frac{1}{n_\omega^2} \left(\frac{n_\omega^2 + 2}{3}\right)\right)^2 \left(\frac{\varepsilon(n_\omega^2 + 2)}{n_\omega^2 + 2\varepsilon}\right)$.

We have not yet defined which component of the refractive index we are considering at the optical frequency of interest. We are also assuming that the hyperpolarizability tensor, β , is dom-

inated by the β_{zzz} component, where the z axis is defined by the dipole moment of the chromophore. The term, $g(\omega)$, contains the Lorentz-Onsager local field factors, f_ω^2 , f_o , which depend on the dielectric constant and refractive indices (n_ω is the appropriate index at the frequency of interest, and n_∞ is the index extrapolated to long wavelength). The specific refractive index elements are dependent on the centrosymmetric order parameters and the mode for which the EO response is being measured. However, the ratio of terms insures that the dependence on the exact values of the refractive index are muted.

We also note here that the order parameters are functions of the positions of the chromophores in the narrowest waveguides. The presence of the electrode walls causes chromophores near the surface to orient with their long axis pointing in the plane of the walls of the slot or electrodes. This introduces a large non-zero, usually negative, centrosymmetric order parameter near the walls, and the acentric order parameter vanishes, (see Figure 5). In the interior of the slot (waveguide), the poling-induced acentric order parameter dominates and the centrosymmetric order parameter tends to be much smaller (in magnitude) than near the walls. The spatial distribution of order parameters can lead to a non-uniform EO response. Such distributions and the slot/waveguide width dependence should be taken into account when determining the position of chromophores with respect to the physical locations of both the modulation field and the optical field.

The direct measurement of r_{33} on μm -thick films is probably best done routinely with the Teng-Man method [89], wherein the reflected optical field is shifted in phase with respect to the incident field due to the refractive index of the OEO material that is modulated by an RF field (in the poling direction), inducing elliptical polarization due to different magnitudes of the index change for s and p-polarized light, for which the electro-optic activity is obtained from the change in phase angle. r_{33} can be measured *in situ* during poling or after the material has been poled.

Both the Teng-Man (bulk material) method and measurements in nanoscale devices using Mach-Zehnder interferometry rely on similar concepts. The RF field introduces a phase delay in the optical field as it passes through an ordered EO material. The phase delay is directly related to the index of refraction of the EO material at the wavelength of the optical field.

$$\begin{aligned} \Delta\phi &= \frac{2\pi L}{\lambda} (n_s(E_{RF}) - n_s(0)) \\ &= \frac{2\pi L}{\lambda} \hat{e}_{opt}^\dagger * (\Delta n) * \hat{e}_{opt} \end{aligned} \quad (3)$$

The phase shift, $\Delta\phi$, of the optical signal is related to the change in the index of refraction, $\Delta n = n_s(E_{RF}) - n_s(0)$, and that change is taken with respect to the RF modulation field, E_{RF} , being off. Thus the phase shift seen by the optical signal is due to the presence of the RF signal, which is taken to be along z , or k : $E_{RF} = E_k$. Δn is a three by three, real symmetric, tensor. The frequency of the RF signal is not particularly significant for measurement purposes as the change in refractive index, Δn , is defined for the optical field propagating through the waveguide. However, in practice, the frequency range for the RF when

measuring Γ_{33} in the bulk is generally in the kHz range; when using the similar material in a POH device, the RF frequency can be in the GHz range. The \hat{e}_{opt} is the unit vector of the E field of the optical signal. The change in index of refraction is related to the EO coefficient, \tilde{r} by definition by:

$$\Delta n = \frac{1}{2} n^{-1} \varepsilon \tilde{r} \varepsilon E_k \quad (4)$$

and depends on the refractive index (and associated dielectric function) of the EO material, where the dielectric function is defined as $\varepsilon = (n + ik)^2$, with k as the imaginary (absorptive) component.

When the TM mode of the waveguide is excited, the E field of the optical signal points in the direction from one electrode plate to the other (coincident with the E field of the RF modulation) and so the E field of the light is experiencing the extraordinary component of the refractive index, n_e along the direction that the chromophores were poled. When the TE mode is excited the E field is perpendicular to the line between the electrodes and so the relevant index of refraction is the ordinary component, n_o . In the Teng-Man measurement (and linear optical measurements, such as VASE or VAPRAS [90]) these are referred to as the P and S polarized light fields, respectively.

We now define the relation between the components of the refractive index tensor, n , and the order parameters. The centrosymmetric order parameter is also proportional to the poling field strength and related to the acentric order parameter by way of the symmetry and rotational dimensionality of the chromophores. The linear optical parameters (such as n, k, ε) are insensitive to the sign of the acentric order parameter; a 180° rotation leaves such quantities unchanged. Therefore, only $\langle P_2 \rangle$ is important to these properties. Moreover, the poling-induced order is thought to start with an isotropic distribution. The inherent underlying anisotropy of the refractive index of a single molecule (or ordered crystal of molecules) is described by the tensor, n . The refractive index of YLD124, for example, is characterized by a nearly-axial tensor with components n_{\parallel} and n_{\perp} and is nearly in the frame of the EO tensor (β) (it is only 4 degrees off). The anisotropic ratio of this tensor is

$$s = \frac{n_{\parallel} - n_{\perp}}{n_{\parallel} + 2n_{\perp}} \quad (5)$$

The average value, which should be observed prior to poling, is: $n_{iso} = \frac{1}{3}(n_{\parallel} + 2n_{\perp})$. The apparent anisotropy for the refractive index is then: $s\langle P_2 \rangle$. Thus $n_o = n_{iso}(1 - s\langle P_2 \rangle)$ and $n_e = n_{iso}(1 + 2s\langle P_2 \rangle)$. Notice that the extraordinary refractive index increases at the expense of the ordinary index. If the chromophores are also absorbing at this wavelength, then the reduced absorbance, k , is also similarly anisotropic.

We now relate the phase shift to the modulating field. The poling field amplitude is simply the voltage, U , divided by the waveguide width (electrode separation), w , $|E_k| = U/w$. Additionally, one needs to know the overlap of the RF modulation, the optical field and the chromophore concentrations. This overlap is Γ , and is determined by simulations for the fields in the

waveguide.

$$\begin{aligned} \Delta\phi &= \frac{2\pi L}{\lambda} (n_s(E_{RF}) - n_s(0)) \\ &= \frac{2\pi UL}{\lambda w} \Gamma \hat{e}_{opt}^\dagger * \frac{1}{2} n^{-1} \varepsilon \tilde{r}_k \varepsilon * \hat{e}_{opt} \end{aligned} \quad (6)$$

For the case when the phase is shifted so that $\Delta\phi = \pi$, then the voltage is U_π . Assuming there is minimal absorbance, i.e., $k = 0$, and that the refractive index tensor is diagonal in the laboratory frame:

$$1 = \frac{U_\pi L}{\lambda w} \Gamma n_e^3 \tilde{r}_{3,3,k} \text{ and } 1 = \frac{U_\pi L}{\lambda w} \Gamma n_o^3 \tilde{r}_{1,1,k} \quad (7)$$

depending on whether the TM or TE mode is being used, respectively, in the experiment. Sometimes one does not bother to distinguish between n_e and n_{iso} ; the approximation is then:

$$1 = \frac{U_\pi L}{\lambda w} \Gamma n_{iso}^3 \tilde{r}_{3,3,k} \quad (8)$$

The deviation from this approximation under poling is shown in Figure 7, which displays the ratio of $(\frac{n_e}{n_{iso}})^3$ as a function of the poling field for different anisotropy parameters, s . Detailed calculations have shown that the Langevin limit to the centrosymmetric order parameter, as a function of the poling field, is quite adequate to provide qualitative insight into the poling field dependence of the ratio. Therefore, we can provide analytic forms to aid the understanding of this term on measuring $U_\pi L$ or inferring, correctly, an accurate estimate to $\tilde{r}_{3,3,k}$.

$$\frac{n_e}{n_{iso}} = (1 + 2s \langle P_2 \rangle) \text{ and } \langle P_2 \rangle = 1 + \frac{3}{f} \left(\frac{1}{f} - \coth(f) \right) \quad (9)$$

where $f = (\frac{3\varepsilon}{n_\infty^2 + 2\varepsilon}) \frac{\mu E_p}{kT}$.

The primary dependence of $\langle P_2 \rangle$ on the poling field is quadratic (at low f : $\langle P_2 \rangle \approx \frac{1}{15} f^2$); and the $\frac{n_e}{n_{iso}}$ factor is cubed in the phase shift expression. Therefore, the correction ratio has, in principle, a 6th power dependence on the field. For low fields and low order, this correction is generally not needed. However, if the material has large centrosymmetric order (as is a result for reduced dimensional systems) or large poling voltages the effects of this term can be seen (Figure 7).

ACKNOWLEDGMENT

Any opinions, findings, and conclusions or recommendations expressed in this communication are those of the authors and do not necessarily reflect the views of the National Science Foundation. The authors wish to particularly thank their collaborators at the Karlsruhe Institute of Technology (Prof. Dr. Christian Koos and his students and postdoctoral fellows) for many helpful discussions.

REFERENCES

- [1] A. Chen and E. J. Murphy, *Broadband Optical Modulators: Science, Technology, and Applications*. Boca Raton, FL, USA: CRC Press, 2012.
- [2] P. J. Winzer, C. J. Chang-Hasnain, A. E. Willner, R. C. Alferness, R. W. Tkach, and T. G. Giallorenzi, "A third of a century of lightwave technology: January 1983-April 2016," *J. Lightw. Technol.*, vol. 34, no. 9, pp. 2079–2084, May 2016.

- [3] J. S. Orcutt *et al.*, "Open foundry platform for high-performance electronic-photonics integration," *Opt. Express*, vol. 20, no. 11, pp. 12222–12232, May 2012.
- [4] Q. Xu, B. Schmidt, S. Pradhan, and M. Lipson, "Micrometre-scale silicon electro-optic modulator," *Nature*, vol. 435, no. 7040, pp. 325–327, May 2005.
- [5] B. Jalali and S. Fathpour, "Silicon photonics," *J. Lightw. Technol.*, vol. 24, no. 12, pp. 4600–4615, Dec. 2006.
- [6] G. T. Reed, G. Mashanovich, F. Y. Gardes, and D. J. Thomson, "Silicon optical modulators," *Nature Photon.*, vol. 4, no. 8, pp. 518–526, Jul. 2010.
- [7] P. Dong, C. Xie, L. Chen, L. Buhl, and Y. Chen, "112-Gb/s monolithic PDM-QPSK modulator in silicon," *Opt. Express*, vol. 20, no. 26, pp. B624–B629, Dec. 2012.
- [8] D. Thomson *et al.*, "Roadmap on silicon photonics," *J. Opt.*, vol. 18, no. 7, Jun. 2016, Art. no. 073003.
- [9] P. Dong, X. Liu, S. Chandrasekhar, L. L. Buhl, R. Aroca, and Y.-K. Chen, "Monolithic silicon photonic integrated circuits for compact 100+ Gb/s coherent optical receivers and transmitters," *IEEE J. Sel. Topics Quantum Electron.*, vol. 20, no. 4, Jul./Aug. 2014, Art. no. 6100108.
- [10] T. Vallaitis *et al.*, "Optical properties of highly nonlinear silicon-organic hybrid (SOH) waveguide geometries," *Opt. Express*, vol. 17, no. 20, pp. 17357–17368, Sep. 2009.
- [11] J. Leuthold *et al.*, "Silicon organic hybrid technology—A platform for practical nonlinear optics," *Proc. IEEE*, vol. 97, no. 7, pp. 1304–1316, Jul. 2009.
- [12] C. Koos *et al.*, "All-optical high-speed signal processing with silicon-organic hybrid slot waveguides," *Nature Photon.*, vol. 3, pp. 216–219, Mar. 2009.
- [13] J. Takayasu *et al.*, "A hybrid electrooptic microring resonator-based $1 \times 4 \times 1$ ROADM for wafer scale optical interconnections," *J. Lightw. Technol.*, vol. 27, no. 4, pp. 440–448, Feb. 2009.
- [14] M. Gould *et al.*, "Silicon-polymer hybrid slot waveguide ring-resonator modulator," *Opt. Express*, vol. 19, no. 5, pp. 3952–3961, Feb. 2011.
- [15] R. Palmer *et al.*, "Low power Mach-Zehnder modulator in silicon-organic hybrid technology," *IEEE Photon. Technol. Lett.*, vol. 25, no. 13, pp. 1226–1229, Jul. 2013.
- [16] L. Alloati *et al.*, "100 GHz silicon-organic hybrid modulator," *Light, Sci. Appl.*, vol. 3, May 2014, Art. no. e173.
- [17] C. Weimann *et al.*, "Silicon-organic hybrid (SOH) frequency comb sources for terabit/s data transmission," *Opt. Express*, vol. 22, no. 3, pp. 3629–3637, Feb. 2014.
- [18] R. Palmer *et al.*, "High-speed, low drive-voltage silicon-organic hybrid modulator based on a binary-chromophore electro-optic material," *J. Lightw. Technol.*, vol. 32, no. 16, pp. 2726–2734, Aug. 2014.
- [19] M. Lauer mann *et al.*, "Low-power silicon-organic hybrid (SOH) modulators for advanced modulation formats," *Opt. Express*, vol. 22, no. 24, pp. 29927–29936, Dec. 2014.
- [20] S. Wolf *et al.*, "DAC-less amplifier-less generation and transmission of QAM signals using sub-volt silicon-organic hybrid modulators," *J. Lightw. Technol.*, vol. 33, no. 7, pp. 1425–1432, Apr. 2015.
- [21] S. Koeber *et al.*, "Femtojoule electro-optic modulation using a silicon-organic hybrid device," *Light, Sci. Appl.*, vol. 4, no. 2, Feb. 2015, Art. no. e255.
- [22] M. Lauer mann *et al.*, "40 Gbd 16QAM signaling at 160 Gbit/s in a silicon-organic hybrid modulator," *J. Lightw. Technol.*, vol. 33, no. 6, pp. 1210–1216, Mar. 2015.
- [23] M. Lauer mann *et al.*, "High-speed and low power silicon-organic hybrid modulators for advanced modulation formats," *Proc. SPIE*, vol. 9516, 2015, Art. no. 951607.
- [24] C. Koos *et al.*, "Silicon-organic hybrid (SOH) and plasmonic-organic hybrid (POH) integration," *J. Lightw. Technol.*, vol. 34, no. 2, pp. 256–268, Jan. 2016.
- [25] M. Lauer mann *et al.*, "Integrated optical frequency shifter in silicon-organic hybrid (SOH) technology," *Opt. Express*, vol. 24, no. 11, pp. 11694–11707, May 2016.
- [26] E. Ozbay, "Plasmonics: Merging photonics and electronics at nanoscale dimensions," *Science*, vol. 311, no. 5758, pp. 189–193, Jan. 2006.
- [27] J. A. Dionne, K. Diest, L. A. Sweatlock, and H. A. Atwater, "PlasMOSTor: A metal-oxide-Si field effect plasmonic modulator," *Nano Lett.*, vol. 9, no. 2, pp. 897–902, Jan. 2009.
- [28] D. K. Gramonev and S. L. Bozhevolnyi, "Plasmonics beyond the diffraction limit," *Nature Photon.*, vol. 4, pp. 83–91, Jan. 2010.
- [29] A. Kriesch, S. P. Birggs, D. Ploss, H. Pfeifer, H. A. Atwater, and U. Perschel, "Functional plasmonic nanocircuits and low insertion and propagation losses," *Nano Lett.*, vol. 13, no. 9, pp. 4539–4545, Aug. 2013.
- [30] A. V. Krasavin and A. V. Zayats, "Active nanophotonic circuitry based on dielectric-loaded plasmonic waveguides," *Adv. Opt. Mater.*, vol. 3, no. 12, pp. 1662–1690, Dec. 2015.
- [31] N. Kinsey, M. Ferrera, V. M. Shalaev, and A. Boltasseva, "Examining nanophotonics for integrated hybrid systems: A review of plasmonic interconnects and modulators using traditional and alternative materials," *J. Opt. Soc. Amer. B*, vol. 32, no. 1, pp. 121–142, Jan. 2015.
- [32] A. Melikyan *et al.*, "High-speed plasmonic phase modulators," *Nature Photon.*, vol. 8, pp. 229–233, Feb. 2014.
- [33] W. Heni *et al.*, "108 Gbit/s plasmonic Mach-Zehnder modulator with >70 GHz electrical bandwidth," *J. Lightw. Technol.*, vol. 34, no. 2, pp. 393–400, Jan. 2015.
- [34] A. Melikyan *et al.*, "Plasmonic-organic hybrid (POH) modulators for OOK and BPSK signaling at 40 Gbit/s," *Opt. Express*, vol. 23, no. 8, pp. 9938–9946, Apr. 2015.
- [35] C. Haffner *et al.*, "All-plasmonic high-speed Mach-Zehnder modulator enabling optical high-speed communications at the microscale," *Nature Photon.*, vol. 9, no. 8, pp. 525–528, Jul. 2015.
- [36] W. Heni *et al.*, "High speed plasmonic modulator array enabling dense optical interconnect solutions," *Opt. Express*, vol. 23, no. 23, pp. 29746–29757, Nov. 2015.
- [37] Y. Salamin *et al.*, "Direct conversion of free space millimeter waves to optical domain by plasmonic modulator antenna," *Nano Lett.*, vol. 15, no. 12, pp. 8342–8346, Nov. 2015.
- [38] Y. Salamin *et al.*, "Direct RF-to-optical detection by plasmonic modulator integrated into a four-leaf-clover antenna," in *Proc. Conf. Lasers Electro-Opt.*, 2016, Paper SM1E.6.
- [39] C. Haffner *et al.*, "Plasmonic organic hybrid modulators—Scaling highest speed photonics to the microscale," *Proc. IEEE*, vol. 104, no. 12, pp. 2362–2379, Dec. 2016.
- [40] R. Bonjour *et al.*, "Plasmonic phased array feeder enabling ultra-fast beam steering at millimeter waves," *Opt. Express*, vol. 24, no. 22, pp. 25608–25618, Oct. 2016.
- [41] W. Heni *et al.*, "Nonlinearities of organic electro-optic materials in nanoscale slots and the implications for the optimum modulator design," *Opt. Express*, vol. 25, no. 3, pp. 2627–2653, Feb. 2017.
- [42] C. Hoessbacher *et al.*, "Plasmonic modulator with >170 GHz bandwidth demonstrated at 100 Gbd NRZ," *Opt. Express*, vol. 25, no. 3, pp. 1762–1768, Feb. 2017.
- [43] W. Heni *et al.*, "Silicon-organic and plasmonic-organic hybrid photonics," *ACS Photon.*, vol. 4, no. 7, pp. 1576–1590, Jun. 2017.
- [44] C. Hoessbacher *et al.*, "Optical interconnect solution with plasmonic modulator and Ge photodetector array," *IEEE Photon. Technol. Lett.*, vol. 29, no. 21, pp. 1760–1763, Nov. 2017.
- [45] C. Haffner *et al.*, "Harnessing nonlinearities near material absorption resonances for reducing losses in plasmonic modulators," *Opt. Mater. Express*, vol. 7, no. 7, pp. 2168–2181, Jul. 2017.
- [46] M. Ayata *et al.*, "High-speed plasmonic modulator in a single metal layer," *Science*, vol. 358, no. 6363, pp. 630–632, Nov. 2017.
- [47] C. Haffner *et al.*, "Low loss plasmon-assisted electro-optic modulator," *Nature*, vol. 556, no. 7702, pp. 483–486, Apr. 2018.
- [48] I.-C. Benea-Chelmsu *et al.*, "Three dimensional, phase modulator at telecom wavelength acting as terahertz detector with an electro-optic bandwidth of 1.25 terahertz," *ACS Photon.*, vol. 5, no. 4, pp. 1398–1403, Feb. 2018.
- [49] D. L. Elder *et al.*, "Multi-scale, theory-assisted, nano-engineering of plasmonic-organic hybrid electro-optic device performance," *Proc. SPIE*, vol. 10529, 2018, Art. no. 105290K.
- [50] B. Baeuerle *et al.*, "Driver-less sub $1 V_{DD}$ operation of a plasmonic-organic hybrid modulator at 100 Gbd NRZ," in *Proc. Opt. Fiber Commun. Conf.*, San Diego, CA, USA, Mar. 11–15, 2018, Paper M2I.1.
- [51] W. Heni *et al.*, "100 Gbd plasmonic IQ modulator," in *Proc. Conf. Lasers Electro-Opt.*, San Jose, CA, USA, May 13–18, 2018, Paper SM1I.4.
- [52] C. Haffner *et al.*, "Bypassing loss in plasmonic modulator," in *Proc. Conf. Lasers Electro-Opt.*, 2018, Paper FTh4H.1.
- [53] B. Baeuerle *et al.*, "Plasmonic-organic hybrid modulators for optical interconnects beyond 100 G/λ," in *Proc. Conf. Lasers Electro-Opt.*, 2018, Paper SM4B.1.
- [54] J. Leuthold *et al.*, "Plasmonics for communications," in *Proc. Opt. Fiber Commun. Conf.*, 2018, Paper M3G.2.
- [55] M. Soljacic, S. G. Johnson, S. H. Fan, M. Ibanescu, E. Ippen, and J. D. Joannopoulos, "Photonic-crystal slow-light enhancement of nonlinear phase sensitivity," *J. Opt. Soc. Amer. B*, vol. 19, no. 9, pp. 2052–2059, Sep. 2002.

- [56] Y. A. Vlasov, M. O'Boyle, H. F. Hamann, and S. J. McNab, "Active control of slow light on a chip with photonic crystal waveguides," *Nature*, vol. 438, pp. 65–66, Nov. 2005.
- [57] J. H. Wulbern, A. Petrov, and M. Eich, "Electro-optical modulator in a polymer-infiltrated silicon slotted photonic crystal waveguide heterostructure resonator," *Opt. Express*, vol. 17, no. 1, pp. 304–313, Jan. 2009.
- [58] C. Y. Lin *et al.*, "Electro-optic polymer infiltrated silicon photonic crystal slot waveguide modulator with 23 dB slow light enhancement," *Appl. Phys. Lett.*, vol. 97, no. 9, Aug. 2010, Art. no. 093304.
- [59] X. L. Wang, C. Y. Lin, S. Chakravarty, J. D. Luo, A. K.-Y. Jen, and R. T. Chen, "Effective in-device $r(33)$ of 735 pm/V on electro-optic polymer infiltrated silicon photonic crystal slot waveguides," *Opt. Lett.*, vol. 36, no. 6, pp. 882–884, Mar. 2011.
- [60] M. Notomi *et al.*, "Low-power nanophotonic devices based on photonic crystals towards dense photonic network on chip," *IET Circuits, Devices Syst.*, vol. 5, pp. 84–93, 2011.
- [61] X. Zhang *et al.*, "High performance optical modulator based on electro-optic polymer filled silicon slot photonic crystal waveguide," *J. Lightw. Technol.*, vol. 34, no. 12, pp. 2941–2951, Jun. 2016.
- [62] L. R. Dalton, P. Gunter, M. Jazbinsek, O.-P. Kwon, and P. A. Sullivan, *Organic Electro-Optics and Photonics: Molecules, Polymers, and Crystals*. Cambridge, U.K.: Cambridge Univ. Press, 2015.
- [63] L. R. Dalton, P. A. Sullivan, and D. H. Bale, "Electric field poled organic electro-optic materials: State of the art and future prospects," *Chem. Rev.*, vol. 110, no. 1, pp. 25–55, Jan. 2010.
- [64] Z. Shi *et al.*, "Controlled Diels-Alder reactions used to incorporate highly efficient polyenic chromophores into maleimide-containing side-chain polymers for electro-optics," *Macromolecules*, vol. 42, no. 7, pp. 2438–2445, Mar. 2009.
- [65] Z. Shi *et al.*, "Tuning the kinetics and energetics of Diels-Alder cycloaddition reactions to improve poling efficiency and thermal stability of high-temperature cross-linked electro-optic polymers," *Chem. Mater.*, vol. 22, no. 19, pp. 5601–5608, Sep. 2010.
- [66] R. Dinu *et al.*, "Environmental stress testing of electro-optic polymer modulators," *J. Lightw. Technol.*, vol. 27, no. 11, pp. 1527–1532, Apr. 2009.
- [67] D. M. Rezzonico *et al.*, "Photostability studies of π -conjugated chromophores with resonant and nonresonant light excitation for long-life polymeric telecommunication devices," *J. Opt. Soc. Amer. B*, vol. 24, no. 9, pp. 2199–2207, Sep. 2007.
- [68] A. F. Tillack, "Electro-optic material design criteria from condensed matter simulations using the level-of-detail coarse-graining approach," Ph.D. dissertation, Dept. Chemistry, Univ. Washington, Seattle, WA, USA, 2015.
- [69] A. F. Tillack, L. E. Johnson, M. Rawal, L. R. Dalton, and B. H. Robinson, "Modeling chromophore order: A guide for improving EO performance," *MRS Online Proc. Library*, vol. 1698, Aug. 2014, Art. no. mrrs14-1698-ijj08-05.
- [70] A. F. Tillack and B. H. Robinson, "Toward optimal EO response from ONLO chromophores: A statistical mechanics study of optimizing shape," *J. Opt. Soc. Amer. B*, vol. 33, no. 12, pp. E121–E129, Dec. 2016.
- [71] S. J. Benight *et al.*, "Reduced dimensionality in organic electro-optic materials: Theory and defined order," *J. Phys. Chem. B*, vol. 114, no. 37, pp. 11949–11956, Sep. 2010.
- [72] L. R. Dalton *et al.*, "Systematic nanoengineering of soft matter organic electro-optic materials," *Chem. Mater.*, vol. 23, no. 3, pp. 430–445, Nov. 2010.
- [73] B. H. Robinson, L. E. Johnson, and B. E. Eichinger, "Relation of system dimensionality and order parameters," *J. Phys. Chem. B*, vol. 119, no. 7, pp. 3205–3212, Jan. 2015.
- [74] B. C. Olbricht *et al.*, "Laser-assisted poling of binary chromophore materials," *J. Phys. Chem. C*, vol. 112, no. 21, pp. 7983–7988, May 2008.
- [75] L. E. Johnson, S. J. Benight, R. Barnes, and B. H. Robinson, "Dielectric and phase behavior of dipolar spheruloids," *J. Phys. Chem. B*, vol. 119, no. 16, pp. 5240–5250, Mar. 2015.
- [76] A. F. Tillack and B. H. Robinson, "Simple model for the benzene hexafluorobenzene interaction," *J. Phys. Chem. B*, vol. 121, no. 25, pp. 6184–6188, Jun. 2017.
- [77] K. Garrett *et al.*, "Optimum exchange for calculation of excitation energies and hyperpolarizabilities of organic electro-optic chromophores," *J. Chem. Theory Comput.*, vol. 10, no. 9, pp. 3821–3831, Aug. 2014.
- [78] L. E. Johnson, L. R. Dalton, and B. H. Robinson, "Optimizing calculations of electronic excitations and relative hyperpolarizabilities of electrooptic chromophores," *Accounts Chem. Res.*, vol. 47, no. 11, pp. 3258–3265, Jun. 2014.
- [79] D. H. Bale *et al.*, "Dielectric dependence of the first molecular hyperpolarizability for electro-optic chromophores," *J. Phys. Chem. B*, vol. 115, pp. 3505–3513, Mar. 2011.
- [80] A. A. Kocherzhenko, X. A. Sosa Vazquez, J. M. Milanese, and C. M. Isborn, "Absorption spectra for disordered aggregates of chromophores using the exciton model," *J. Chem. Theory Comput.*, vol. 13, no. 8, pp. 3787–3801, Jul. 2017.
- [81] A. Emboras *et al.*, "Atomic scale plasmonic switch," *Nano Lett.*, vol. 16, no. 1, pp. 709–714, Jan. 2016.
- [82] R. Bonjour *et al.*, "Ultra-fast millimeter wave beam steering," *IEEE J. Quantum Electron.*, vol. 52, no. 1, Jan. 2016, Art. no. 0600708.
- [83] W. Jin *et al.*, "Structure-function relationship exploration for enhanced thermal stability and electro-optic activity in monolithic organic NLO chromophores," *J. Mater. Chem. C*, vol. 4, no. 15, pp. 3119–3124, Mar. 2016.
- [84] G. Kresse and J. Hafner, "Ab initio molecular dynamics for liquid metals," *Phys. Rev. B*, vol. 47, no. 1, pp. 558–561, Jan. 1993.
- [85] G. Kresse and D. Joubert, "From ultrasoft pseudopotentials to the projector augmented-wave method," *Phys. Rev. B*, vol. 59, no. 3, pp. 1758–1775, Jan. 1999.
- [86] J. L. Oudar and D. S. Chemla, "Hyperpolarizabilities of the nitroanilines and their relations to the excited state dipole moment," *J. Chem. Phys.*, vol. 66, no. 6, pp. 2664–2668, Mar. 1977.
- [87] K. D. Singer, M. G. Kuzyk, and J. E. Sohn, "Second-order nonlinear-optical processes in orientationally ordered materials: Relationship between molecular and macroscopic properties," *J. Opt. Soc. Amer. B*, vol. 4, no. 6, pp. 968–976, Jun. 1987.
- [88] D. Paschoal and H. F. Dos Santos, "Computational protocol to predict hyperpolarizabilities of large π -conjugated organic push-pull molecules," *Organic Electron.*, vol. 28, pp. 111–117, Jan. 2016.
- [89] C. C. Teng and H. T. Man, "Simple reflection technique for measuring the electro-optic coefficient of poled polymers," *Appl. Phys. Lett.*, vol. 56, no. 18, pp. 1734–1737, Feb. 1990.
- [90] B. C. Olbricht *et al.*, "Measuring order in contact-poled organic electrooptic materials with variable angle polarization-referenced absorption spectroscopy (VAPRAS)," *J. Phys. Chem. B*, vol. 115, no. 2, pp. 231–241, Dec. 2011.

Authors' biographies not available at the time of publication.